Comput Mech (2012) 49:337–355
DOI 10.1007/s00466-011-0643-0

ORIGINAL PAPER

An embedded atom hyperelastic constitutive model and multiscale cohesive finite element method

Minghua He · Shaofan Li

Received: 20 June 2011 / Accepted: 21 August 2011 / Published online: 20 September 2011

Abstract Based on embedded atom method (EAM), an embedded atom hyperelastic (EAH) constitutive model is developed. The proposed EAH constitutive model provides a multiscale formalism to determine mesoscale or macroscale material behavior by atomistic information. By combining the EAH with cohesive zone model (CZM), a multiscale embedded atom cohesive finite element model (EA-cohesive FEM) is developed for simulating failure of materials at mesoscale and macroscale, e.g. fracture and crack propagation etc. Based on EAH, the EA-cohesive FEM applies the Cauchy-Born rule to calculate mesoscale or macroscale material response for bulk elements. Within the cohesive zone, a generalized Cauchy-Born rule is applied to find the effective normal and tangential traction-separation cohesive laws of EAH material. Since the EAM is a realistic semi-empirical interatomic potential formalism, the EAH constitutive model and the EA-cohesive FEM are physically meaningful when it is compared with experimental data. The proposed EA-cohesive FEM is validated by comparing the simulation results with the results of large scale molecular dynamics simulation. Simulation result of dynamic crack propagation is presented to demonstrate the capacity of EA-cohesive FEM in capturing the dynamic fracture.

National Natural Science Foundation of China (Grant 50878117; Key Project Grant 51038006); China Scholarship Council Project (M.H. HE-2009621076); NSF (Grant No. CMMI-0800744).

M. He
Department of Civil Engineering, Tsinghua University, Beijing 100084, China
e-mail: hmh03@mails.tsinghua.edu.cn

S. Li (✉)
Department of Civil and Environmental Engineering, University of California, Berkeley, CA 94720, USA
e-mail: shaofan@berkeley.edu

Keywords Cohesive zone model · Embedded atom method (EAM) · EA-cohesive FEM · Fracture · Multiscale simulation

1 Introduction

Material failures in solids, e.g. fracture and crack propagation in metals, are typical multiscale phenomena, in which interactions among different spatial and temporal scales are dominant and pervasive e.g. see Geubelle et al. [15]. Though *Ab initio* methods or first principle based calculations are desirable, it is hardly practical to use them for a system with large number of atoms [41], because of both computational expense and inherent complexity of a large atomistic ensemble system. With obvious efficiency in comparison with *Ab initio* calculations, molecular-dynamics (MD) or Monte Carlo (MC) method makes a compromise in accuracy [37], but a substantial gain in speed and efficiency. To compensate accuracy, the embedded-atom-method [9,10] provides a better description of interatomic interactions compared with conventional pair potentials [21,22], while retaining computation efficiency. With the embedded atom method (EAM), many defect problems e.g. crack, melting, grain boundary etc. have been successfully investigated in connection with experimental results [11], and the results of first principle based calculations [8]. An appropriate EAM model is usually established based on the database of experimental measurements or first principle based calculations. After the EAM formalism was developed by Daw and Baskes [9], many EAM potentials have been constructed with respect to the specific types of metallic systems. Aiming at describing a wider range of materials, partial background electron densities related to angular momentum contributions from (spdf) electron orbits have been established with respect to the

directionality of the background electron density in the modified EAM [4]. To avoid dealing with the complexity and difficulty of fitting parameters of the modified EAM with experimental data, effort has been made to apply EAM to a wide range materials including FCC [33,41], BCC [23,1], HCP [33]. In particular, by prescribing analytical EAM potential functions, the EAM potentials for materials with FCC, BCC and HCP crystal structures are made as popular as the analytical pairwise potentials.

The state of the art of finite element method has two approaches to model fracture and crack growth: (1) the extended finite element method (X-FEM), which uses a locally enriched interpolation field, e.g. the Heaviside function, at the crack tip and crack surface to represent strong discontinuity [31], and (2) the cohesive zone model [40], which releases and splits the shared FEM nodes between adjacent elements rendering the capacity of describing discontinuity within the existing finite element mesh. The conventional cohesive zone model is based on a mathematical or mechanical interface formalism that provides a set of empirical cohesive laws without looking into the atomistic origin of cohesion and decohesion, e.g. [40]. However, some effort has been made to relate the empirical cohesive relation to experimental measurement data [39]. Nevertheless, a current trend of the cohesive zone model research starts to focus on how to quantify the cohesive zone behavior at multiple length scales with respect to the physical origin of the decohesion such as atomistic and molecular interactions, crystal and grain deformation etc. For example, to investigate the multiscale hierarchical structure of gecko's attachment system, a multiscale cohesive law is formulated in the work of Yao and Gao [42]. In fact, it has become a public consensus now that an ideal approach to form a physics-based cohesive law is to extrapolate constitutive information from atomistic microstructures [6,17,28,32].

To simulate atomistic interaction at small scale, a multiscale cohesive zone model (MCZM) has been developed [36,43], in which finite width cohesive elements are embedded within bulk elements, and material interface cohesive relations are completely determined by atomistic potentials. To capture the depletion nature of the cohesive zone, the depletion potential approach in colloidal physics has been adopted in cohesive elements. However, in this approach, the electron density-independent pairwise potential has been used, which suffers from several fatal shortcomings. For instance, it is not true that the vacancy formation energy is always equal to the cohesive energy as predicted by the pairwise potential approach. Moreover if the pairwise potential is adopted to constitute a Cauchy-Born solid, the induced elastic coefficients of elastic tensor $\mathbf{C}$ for a given orthogonal basis in the stress space always renders the Cauchy relation $C_{12} = C_{44}$, which may not be physical either [11]. On the other hand, the EAM formalism mentioned above takes into account the effects of electron density distribution, which avoids such drawbacks caused from the density-independent atomistic potentials.

In order to simulate material failures in solids, which are intrinsically multiscale phenomena, particular mathematical models on different scales should be considered to capture the essence of physical reality. Each mathematical model of a given scale addresses a physical phenomenon governed by different physical laws over a specific window of length and time. Usually the following scales are distinguished: subatomic scale or scale of quantum mechanical models (electronic structures are introduced and *Ab initio* is needed); atomistic scale or scale of molecular dynamics models (timescale is around 10^{-15} to 10^{-9} s and lengthscale is around 0.1–10 nm; Molecular dynamics, Monte Carlo etc. are appropriate); mesoscale or nanoscale (timescale is around 10^{-8} to 10^{-2} s; lengthscale is around 10–1000 nm; coarse-graining information about groups of atoms and molecules is dominated); macroscale or scale of continuum models (timescale is longer than 0.1 s and lengthscale is longer than 1 μm; FEM is appropriate).

In this work, a multiscale EA-cohesive FEM with an embedded atom hyperelastic (EAH) constitutive model is presented. In the proposed EA-cohesive FEM, the EAH combines the cohesive zone model (CZM) with the EAM potential that is parameterized from the results of first principle calculations and experimental measurements [9,14]. The phrase *multiscale EA-cohesive finite element method* that we use in this paper is referred to the model takes into account physical features from multiple spatial and temporal scales. More precisely, it is a mesoscale model that is enriched by the information from sub-atomic and atomistic scales. Scale separation is the fundamental characteristic of all the existing multiscale methodology. Many problems arising in multiscale analysis are concerned with the interfacing of different mathematical models appropriate at different scales (e.g. quantum, molecular and continuum). Usually we refer those multiscale methods as the con-current multiscale method, whereas in this work. the presented EA-cohesive FEM is aimed at simulating material cohesive behavior on mesoscale or even macroscale by using information from atomistic scale.

With the aid of the EAM formalism, the shortcomings associated with density-independent pairwise potentials are improved, and the EAH constitutive model we proposed is a more realistic coarse-graining constitutive models. Accordingly, more realistic interface cohesive law can be obtained. Based on a given crystalline structure, e.g. FCC, BCC, HCP etc., mesoscale constitutive model can be calculated. This procedure is essentially a molecular dynamics computation that is carried out for only one atom for each element. As a multi-body potential, even for a single atom computation, an EAM based molecular dynamics has to be performed in a supercell of many atoms. Usually, such a supercell is formed by stacking a number of primitive unit cells together [41].

Straightforward application of Cauchy-Born rule can also be found in the so-called Quasi-continuum (QC) method [38], as well as the Virtual Internal Bond model [27]. To link the mesoscale deformation to the microscale lattice deformation efficiently, a generalized Cauchy-Born rule is shown to reduce the computational cost [13].

The paper is organized in seven sections. In Sect. 2 the basic ideas of multiscale cohesive finite element model are discussed, including the decohesion criterion and essential kinematics. Section 3 is focused on deriving the governing equations of multiscale cohesive finite element model and its Galerkin weak formulation. In Sect. 4 an EAH constitutive model is developed. In Sect. 5 the behavior of the EAH constitutive model in bulk element and cohesive zone is discussed. In Sect. 6 numerical examples are presented; Finally in Sect. 7, the presented work is concluded with a few remarks.

The following convention of notation is adopted: Roman and italic letters stand for scalar or scalar fields, and only bold letters stand for vectorial or tensorial fields or variables.

2 Basic ideas of multiscale cohesive finite element model

The original concept of cohesive zone model may be traced back to the work of Barenblatt [2]. However, combining the cohesive zone model with finite element method in engineering computation was made popular by Xu and Needleman [40], which was initially intended to avoid cumbersome FEM re-meshing while simulating fracture by using the finite element method.

A general illustration of the conventional cohesive zone model is shown in Fig. 1. In the conventional cohesive zone model, a pair of discrete cohesive surfaces, which obey certain prescribed cohesive law is introduced. The introduction of the cohesive surfaces allows discontinuity kinematics in finite element solution. It makes the simulation of fracture possible, because the crack-like defect can propagate along the element boundaries under the control by the prescribed cohesive laws.

Traditionally, the prescribed functional cohesive law must be validated with experimental observation to establish a physics-based cohesive zone model. It is necessary, but challenging, in engineering applications to fit the functional form of empirical cohesive law with experimental results. Besides, the empirical cohesive laws are based on the concepts of phenomenological fracture mechanics in which the fracture is categorized as three cleavage fracture modes. In fact, even within the realm of phenomenological fracture mechanics, the conventional cohesive zone model may be still facing troubles in describing mixed mode fracture. Then, the idea of investigating the fundamental material structure offers another possible approach to establish a physics-based

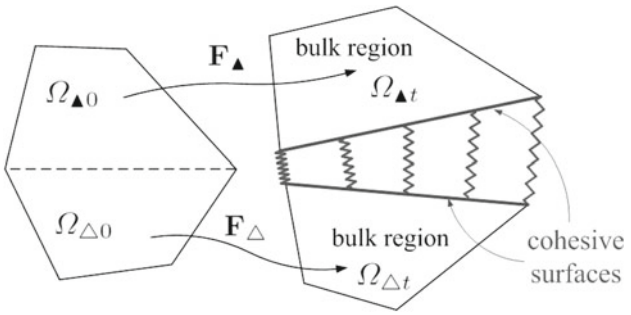

Fig. 1 Schematic illustration of conventional cohesive zone model with cohesive surfaces and prescribed cohesive law

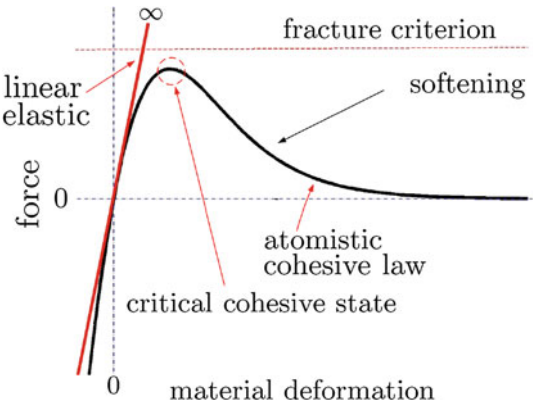

Fig. 2 Schematic conceptual comparison between atomistic cohesive (interaction) law and phenomenological linear elasticity model

cohesive model. It is interesting to notice that the very early cohesive zone model [2] was also motivated by the physics of atomistic interactions.

2.1 Decohesion criterion

In principle, whether or not it is in first principle or phenomenological model, material failure behavior should be considered as a natural material response that can be described in the constitutive model. A complete material constitutive relation should be able to intrinsically or naturally describe material failure without additional failure criterion. For instance, one example of such complete constitutive relations is the atomistic cohesive law (or atomistic interaction) demonstrated in Fig. 2.

However, several well-known idealized phenomenological constitutive models, e.g. linear elastic relation (Hooke's law) or hyperelastic constitutive relation, are not the full-ranged complete material constitutive models, and they only model material behavior in a particular deformation range or stress level. Hence, additional failure criteria (e.g. strength limit, finite stress threshold etc.) are required in order to simulate the whole history of material failure, especially the threshold of failure. In fact, to simulate phenomenological

fracture within the framework of elasticity, a fracture criterion is crucial (as depicted in Fig. 2). Otherwise, the material will never fail no matter how large the stress is, which is in contrary to material behaviors. On the other hand, as mentioned above, in the paradigm of cohesive model such as the atomistic bonding relation, a priori fracture criterion is no longer needed because the failure criterion is intrinsically embedded into the cohesive relation, which is capable of representing the full-ranged material constitutive behavior. Being consistent with experimental observation, from Fig. 2, one may find that during the loading process the material in question can reach the critical cohesive state with finite strength. With a little disturbance alongside loading direction in stress space, the material will fracture because the load resistance capacity drops as the deformation increases.

In general, the mesoscale or macroscale cohesive model in terms of traction and surface separation is a reflection or homogenization of atomistic scale cohesive behavior that originates from atomistic debonding. In other words, the cohesive nature of atomistic behavior is more fundamental than the mesoscale or macroscale cohesive model. Therefore, the atomistic potential can provide a complete description of cohesive constitutive behavior. This is the source of inspiration of the proposed multiscale EA-cohesive FEM and the EAH constitutive model.

2.2 Kinematics of the multiscale cohesive zone model

To develop an atomistic informed mesoscale cohesive zone model, recently Zeng and Li proposed a multiscale cohesive zone model (MCZM) [43]. In the MCZM, the mesoscale cohesive relation between the interface traction and the surface separation is derived from the physically realistic atomistic potential inside the cohesive zone. Hence the cohesive zone in MCZM is a finite volume zone with finite thickness. This is fundamentally different with the conventional cohesive zone model (e.g. that of [40]), where the cohesive zone is a virtual zone with zero thickness, and the interfacial cohesive relation is an empirical formulation that may be prescribed by fitting the the experimental data (e.g. [3]).

It may be noted that in engineering applications, empirical cohesive laws often work well in some cases but do not work well in some other cases. A main reason for such inconsistency, we believe, is because the interface cohesive law is unrelated with bulk material properties such as microstructure anisotropy, damage state (e.g. dislocation density), and even Young's modulus and Poisson's ratio, etc.

In the proposed multiscale EA-cohesive FEM, material failure is viewed as atomistic debonding at atomistic scale, which is described naturally by atomistic potential. It justifies that it is reasonable to describe the cohesive interface separation based on the specific atomistic structure and associated potentials. The main kinematic assumption of the EA-cohesive FEM is that the deformation inside each bulk element is homogeneous, and the unstable nonuniform deformation is confined inside the cohesive zones locally. It implies that the localization is triggered by the assumed atomistic debonding within the cohesive zones.

To calculate nonlinear inhomogeneous deformation inside the cohesive element, the inhomogeneous deformation is considered as a multiscale quantity. Precisely speaking, we may decompose the displacement field within the cohesive element into two scales:

$$\mathbf{u}_{coh} = \overline{\mathbf{u}}_{coh} + \mathbf{u}'_{coh}, \tag{1}$$

where $\overline{\mathbf{u}}_{coh}$ denotes the global homogeneous or coarse-graining displacement field of cohesive zone, whereas $\mathbf{u}'_{coh}$ is the in-homogeneous displacement noise or fine scale displacement fluctuation field of cohesive zone. Thus, the current deformed configuration of cohesive zone can be represented as:

$$\mathbf{x}_{coh} = \overline{\mathbf{x}}_{coh} + \mathbf{u}'_{coh} = \overline{\mathbf{F}}_{coh}\mathbf{X}_{coh} + \mathbf{u}'_{coh}, \tag{2}$$

where $\overline{\mathbf{F}}$ and $\overline{\mathbf{x}}_{coh} = \mathbf{X}_{coh} + \overline{\mathbf{u}}_{coh}$ denote homogeneous coarse-graining deformation gradient and homogenous coarse-graining material position field respectively.

Without loss of generality, we may consider a two dimensional (2D) cohesive zone. In a 2D domain, the cohesive surfaces degenerate to line segments. If the triangle element is used for bulk elements, the finite cohesive zone will have a quadrilateral shape consisting of four boundary edges. To find the average the deformation gradient inside the cohesive zone, an affine mapping method was employed in [43]. Since the deformation inside the bulk element is assumed to be uniform and all the displacement fluctuation or fine scale displacement is confined inside the cohesive element, one can show that the average deformation deformation gradient can be determined by the displacements of the finite element nodes that are on the boundary of the cohesive element. Using the finite element nodal position coordinates as parameters (Fig. 3), the effective deformation gradient of the cohesive zone $\overline{\mathbf{F}}_{coh}$ is given in the component form as follows [43]:

$$\begin{Bmatrix} \overline{F}^{11}_{coh} \\ \overline{F}^{12}_{coh} \\ \overline{F}^{21}_{coh} \\ \overline{F}^{22}_{coh} \end{Bmatrix} = \frac{1}{(ad-cb)} \begin{bmatrix} d & 0 & -b & 0 \\ -c & 0 & a & 0 \\ 0 & d & 0 & -b \\ 0 & -c & 0 & a \end{bmatrix} \begin{Bmatrix} x^+_{l+1} - x^-_l \\ y^+_{l+1} - y^-_l \\ x^+_l - x^-_{l+1} \\ y^+_l - y^-_{l+1} \end{Bmatrix}, \tag{3}$$

where

$$a = X^+_{l+1} - X^-_l, b = Y^+_{l+1} - Y^-_l,$$
$$c = X^+_l - X^-_{l+1}, d = Y^+_l - Y^-_{l+1}.$$

Since inside the cohesive zone the deformation is highly nonlinear, one cannot apply the Cauchy-Born rule to extrapolate

the meso-scale constitutive relation in the cohesive zone. However, the deformation gradient that characterizes the highly nonlinear deformation inside the cohesive zone may be expanded in a Taylor series with respect to a chosen point $\mathbf{X}^*$ and

$$\mathbf{F}_{coh}(\mathbf{X}^*) = \overline{\mathbf{F}}_{coh}$$

such that we may approximate the deformation gradient at an arbitrary point inside the cohesive element as

$$\mathbf{F}_{coh}(\mathbf{X}) = \overline{\mathbf{F}}_{coh} + \frac{\partial \mathbf{F}}{\partial \mathbf{X}}\Big|_{\mathbf{X}^*} \cdot(\mathbf{X}-\mathbf{X}^*) + \frac{1}{2!}\frac{\partial^2 \mathbf{F}}{\partial \mathbf{X}^2}\Big|_{\mathbf{X}^*} : (\mathbf{X}-\mathbf{X}^*)\otimes(\mathbf{X}-\mathbf{X}^*) + \cdots \quad (4)$$

One may note that in fact the quadrilateral element has ability to accommodate one strain gradient components, and however to completely take into account the effects of the strain gradient term one needs the higher order quadrilateral elements. The study of the strain gradient based MCZM will be discussed in a separated paper.

To focus on the multiscale EA-cohesive FEM in this work, we consider using the mean field approximation on deformation gradient, e.g. $\mathbf{F}_{coh}(\mathbf{X}) \approx \overline{\mathbf{F}}_{coh}$. The advantage of such approximation is that it provides a theoretical ground to apply the Cauchy-Born rule [13] to the mean or the average deformation field inside the cohesive zone. Nevertheless, this is an overly simplified approximation that has no restriction of the cohesive zone's nonlinear deformation. In computations, the aspect ratio of the cohesive element is very small (10^{-3} to 10^{-5}), which makes the cohesive element begin stiff. Thus the quadrilateral cohesive element exhibits the so-called locking phenomenon under geometric distortion. In a sense, the mean field approach to cohesive element is equivalent to one point integration, or reduced integration, which helps relieve locking. However, this may cause hour-glass mode for cohesive elements. To assure computational results reliable and to make the calculation physically meaningful, we introduce the following additional restrictions on the deformation field of the cohesive zone to control the hour glass model (see Fig. 4). Consider the bulk element as the triangular constant strain element, and then the point-wise deformation gradient within the bulk element is also a constant two-point tensor, or it only contains coarse scale contribution. As illustrated in Fig. 4, we denote the cohesive zone characteristic vectors as $\mathbf{R}_{h1}$, $\mathbf{R}_{h2}$, $\mathbf{R}_1$ and $\mathbf{R}_2$ in reference configuration, $\mathbf{r}_{h1}$, $\mathbf{r}_{h2}$, $\mathbf{r}_1$ and $\mathbf{r}_2$ in current configuration. As edge vectors, only three of them are independent. To account for the potential separation inside the bulk domain, the separated bulk bodies (reflected by the element) along the cohesive surface are denoted as $\triangle$ and $\blacktriangle$ antithetically. Then the vector mapping within the bulk elements associated with the separated bodies is given by:

$$\mathbf{r}_1 = \mathbf{F}_{\triangle}\mathbf{R}_1, \quad \mathbf{r}_2 = \mathbf{F}_{\blacktriangle}\mathbf{R}_2, \quad (5)$$

where $\mathbf{F}_{\triangle}$ and $\mathbf{F}_{\blacktriangle}$ are the deformation gradients of the bulk element $\Omega_{\blacktriangle t}$ and $\Omega_{\triangle t}$ respectively. In order to assure that the shape of the cohesive zone does not distort severely and stays convex, the triple products of the characteristic vectors must satisfy the first motion restriction given by:

$$[\mathbf{r}_1, \mathbf{r}_{h1}, \widehat{\mathbf{e}}_3] > 0 \quad and \quad [\mathbf{r}_2, \mathbf{r}_{h1}, \widehat{\mathbf{e}}_3] > 0, \quad (6)$$

where $\widehat{\mathbf{e}}_3$ is the normailzed basis orthogonal to the 2D plane. Analogously, to avoid the line segments of the bulk element penetrating each other even if the cohesive zone has become concave, the line segmental vectors must satisfy the second motion restriction given by,

$$[\mathbf{r}_\alpha, \mathbf{r}_{hA}, \widehat{\mathbf{e}}_3] > 0 \quad and \quad [\mathbf{r}_{hA}, \mathbf{r}_\beta, \widehat{\mathbf{e}}_3] > 0, \quad \alpha, \beta, A = 1, 2. \quad (7)$$

The first restriction essentially preserves convexity of the cohesive zone, therefore we term it as *the convexity restriction*. Likewise, the second restriction is aimed at preventing bulk element overlapping and penetrating each other, we thus coin it as *the overlapping restriction*. These restrictions provides additional regularization on the deformation of the cohesive zone when we apply the Cauchy-Born rule to an effective field, which may be relaxed if strain gradient effect or even high order strain gradient effects are considered.

3 Governing equations of EA-cohesive FEM and its Galerkin weak formulation

As depicted in Fig. 5, the structural or material domain is modeled as a multiscale hierarchical system with EAH micro structure in a Lagrangian FEM framwork. The whole domain is discretized by a set of bulk elements (triangular or quadrilateral domains in 2D space; tetrahedral, pentahedron or hexahedral etc. in 3D space) and a distributed network of cohesive zones is introduced. In this work an identical EAH material model based on the same embedded atom potential is implemented to guarantee that both the bulk element and cohesive zone have the same microstructure and material properties. The introduced cohesive zones in the proposed model are not pre-damaged zones or pre-weaken interfaces. In other words, the union set of the bulk regions and cohesive zones performs exactly the same with the whole domain under elastic loading before the critical cohesive state. When the specimen is loaded, the area with higher stress level will reach to the critical cohesive limit earlier than the area with lower stress level. According to the equilibrium requirement, the stress will be redistributed when parts of the specimen domain unload forward on the softening path (e.g. fracture or

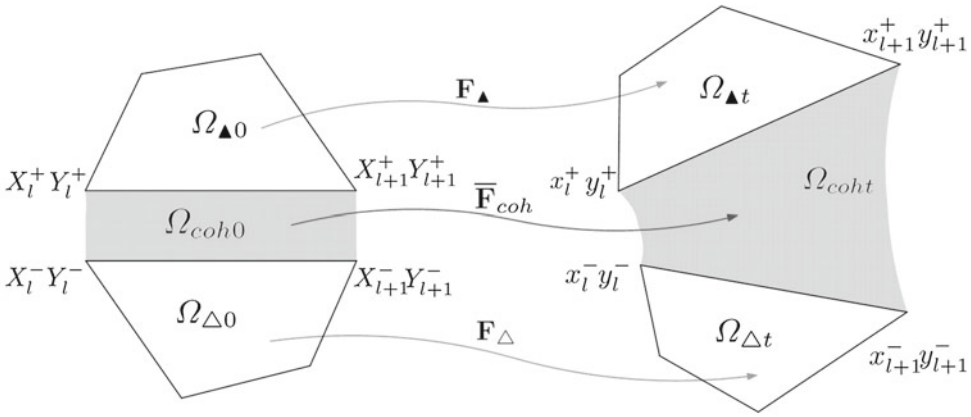

Fig. 3 Effective deformation mapping $\overline{\mathbf{F}}_{coh}$ inside the cohesive element in terms of nodal coordinates

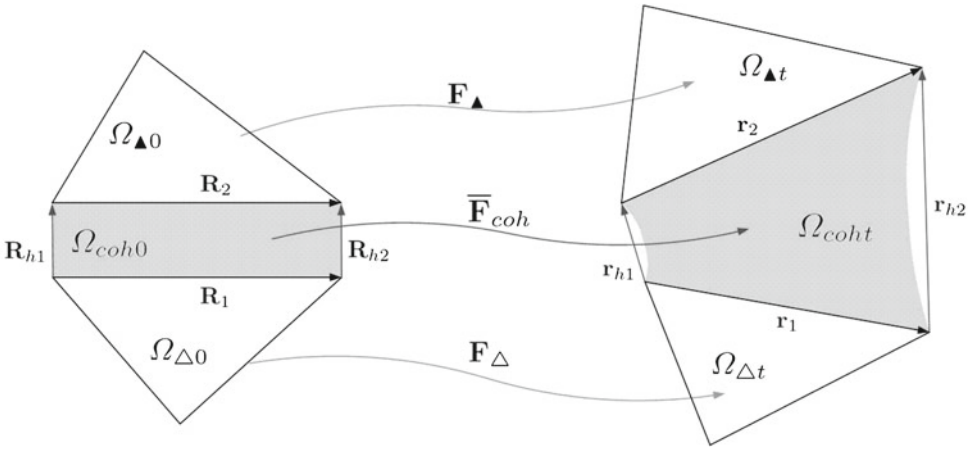

Fig. 4 Parameters needed in the convexity restriction and overlapping restriction on cohesive element to avoid hour-glass mode

yield) and the adjacent parts unload backward on the elastic branch. Here we refer it as the stress redistribution mechanism. In fact, the continuum assumption holds in a region until the material of the region unloads forward on the post-peak softening branch, and there is no pre-defined interface quantities in the system. Whereas in the conventional cohesive zone model a pre-defined physical interface with independent cohesive constitutive relations or cohesive law is embedded along the finite element edges, which often causes abnormal or lower wave speeds in the numerical cohesive continuum (e.g. [40]). Besides, in the proposed multiscale model, when the stress state reaches to a critical cohesive state, the cohesive zone (Ω_{coh0}) automatically switches to an "interface element" so it provides the suitable kinematics to model strong discontinuities in the domain. For the proposed model, though no pre-damaged zones are introduced, a distributed network of cohesive elements associated with a fine finite element discretizaion can also approximate the possible crack path. In physics, though a specimen is made of the same material and no geometric defect is introduced, the specimen may fracture when it is loaded to its ultimate material strength. Likewise, though an identical EAH material is used in both bulk and cohesive regions, the crack nucleates and grows when some regions of the specimen are loaded beyond the critical cohesive state. In order to simulate the crack growth, notches or precracks are introduced in specimen as initial defects. The stress concentration at the precrack tip will leads to higher stress level, and hence initialize fracture in the cohesive zone naturally.

When FEM mesh is fine enough, even if the true crack is passing through the bulk element, one may still get satisfactory result, because the simulated crack within the cohesive element network can provide a good approximation for the real crack. In order to prevent the bulk elements from "further deforming" or becoming fractured in a perfect specimen, one possible way is to truncate the post-peak branch of the atomistic potential of bulk element by only using the stable elastic branch to guarantee the surface separation or fracture occurs in the cohesive element. Generally speaking, perfect specimen doesn't exist and all of the engineering specimens are born with defects (e.g. precrack or notchs etc.). In defected specimen, the stress distribution is not homogenous, and there is stress singularity in the vicinity of crack tip, which makes the cohesive elements lying in the crack growing direction have higher effective stress. According to the equilibrium condition, once the cohesive zones unload forward on

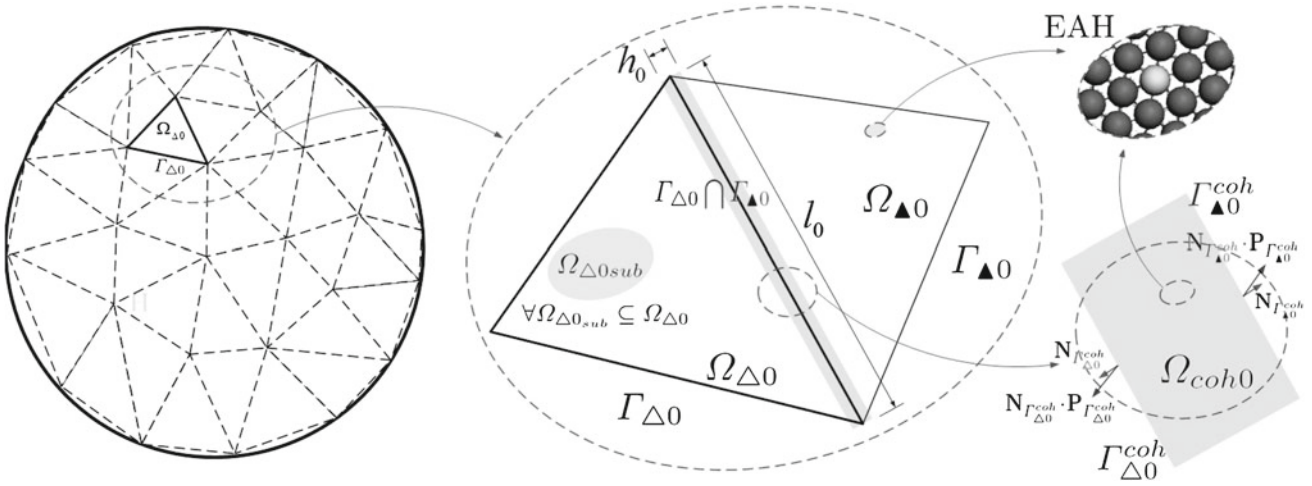

Fig. 5 The multiscale hierarchy system of the proposed multiscale EA-cohesive finite element method

the softening branch, the adjacent bulk elements will unload backward
on the elastic path of EAH constitutive model. It means that the stress will be redistributed in the specimen. When the the cohesive elements reach the critical cohesive state earlier than the adjacent bulk elements, the stress redistribution mechanism will guarantee that the bulk elements unload elastically. The stress redistribution can also make the specimen fractures in the cohesive elements naturally without killing elements artificially.

3.1 Governing equations of EA-cohesive finite element method

The governing equations of the EA-cohesive finite element method may be derived from the balance of linear momentum. Consider an open and connected set $\Omega \subset R^n$ with boundary $\partial\Omega$ in the domain of analysis. Given any subset $\Omega_{\triangle 0}$ with boundary $\Gamma_{\triangle 0}$, the global balance law is employed on any given patch $\Omega_{\triangle 0sub} \subseteq \Omega_{\triangle 0}$ in the reference configuration, and the time derivative with respect to linear momentum $\boldsymbol{l}$ is given by:

$$\dot{\boldsymbol{l}} = \int_{\Gamma_{\triangle 0sub}} \mathbf{t}_0^{n_0} d\Gamma_{\triangle 0} + \int_{\Omega_{\triangle 0sub}} \rho_0 \mathbf{b} d\Omega_{\triangle 0} = \int_{\Omega_{\triangle 0sub}} \rho_0 \mathbf{a} d\Omega_{\triangle 0}, \tag{8}$$

where ρ_0 is the original density, $\mathbf{t}_0^{n0}$ is the traction force with respect to the normal vector $\mathbf{n}_0$, $\mathbf{b}$ is the body force per mass and $\mathbf{a} = \ddot{\mathbf{u}}$ is the acceleration of the deferential volume in question. By invoking the divergence theorem, the balance of linear momentum may be written in a global form as follow,

$$\int_{\Omega_{\triangle 0sub}} \mathrm{Div}(\mathbf{P}) d\Omega_{\triangle 0sub} + \int_{\Omega_{\triangle 0sub}} \rho_0 \mathbf{b} d\Omega_{\triangle 0sub} = \int_{\Omega_{\triangle 0sub}} \rho_0 \mathbf{a} d\Omega_{\triangle 0sub}, \tag{9}$$

where the $\mathbf{P}$ is the first Piola–Kirchhoff stress tensor. Consider the balance of linear momentum for any arbitrary $\Omega_{\triangle 0sub}$ within $\Omega_{\triangle 0}$, the following strong form holds in material point within the sub domain $\Omega_{\triangle 0_{sub}}$,

$$\mathrm{Div}\mathbf{P} + \rho_0 \mathbf{b} - \rho_0 \mathbf{a} = 0, \forall \Omega_{\triangle 0_{sub}} \subseteq \Omega_{\triangle 0}. \tag{10}$$

By the definition $\mathbf{u} = \mathbf{x} - \mathbf{X}$, and the boundary conditions with respect to displacement $\mathbf{u}$ and traction $\mathbf{t}$ are given by

$$\mathbf{u} = \widetilde{\mathbf{u}} \qquad \text{on } \Gamma^u_{\triangle 0} = \partial_u \Omega_{\triangle 0}, \tag{11}$$

$$\mathbf{P} \cdot \mathbf{N} = \widetilde{\mathbf{T}} \qquad \text{on } \Gamma^t_{\triangle 0} = \partial_t \Omega_{\triangle 0}. \tag{12}$$

For a given $\Omega_{\triangle 0}$, we denote one of its adjacent subsets as $\Omega_{\blacktriangle 0}$ respectively. In conventional cohesive finite elements, These two neighbor subdomains share the part of their boundaries, which is denoted as $\Gamma_{\triangle 0} \bigcap \Gamma_{\blacktriangle 0}$. In EA-cohesive FEM these two boundaries are connected by a finite size cohesive element. In other word, these two boundaries are separated by constitutive width (2D space) or thickness (3D space) h_0 (see Fig. 5) of the cohesive zone, and they form a pair of crack surfaces after the corresponding cohesive strength vanishes. For convenience, the boundaries associated with the cohesive surfaces are denoted as $\Gamma^{coh}_{\triangle 0}$ and $\Gamma^{coh}_{\blacktriangle 0}$ respectively. On the reference configuration, the length of the cohesive surfaces $\Gamma^{coh}_{\triangle 0}$ and $\Gamma^{coh}_{\blacktriangle 0}$ is denoted by l_0. If we assume there is inertia inside the cohesive zone, the traction forces should satisfy

$$\mathbf{N}_{\Gamma^{coh}_{\triangle 0}} \cdot \mathbf{P}_{\Gamma^{coh}_{\triangle 0}} + \mathbf{N}_{\Gamma^{coh}_{\blacktriangle 0}} \cdot \mathbf{P}_{\Gamma^{coh}_{\blacktriangle 0}} + h_0 \rho_0 \mathbf{b}_{coh} = h_0 \rho_0 \mathbf{a}, \quad on \quad \Gamma^{coh}_{\triangle 0}, \Gamma^{coh}_{\blacktriangle 0}, \tag{13}$$

where ρ_0, $\mathbf{N}_{\Gamma^{coh}_{\triangle 0}}$ and $\mathbf{N}_{\Gamma^{coh}_{\blacktriangle 0}}$ denote the initial density of cohesive zone, outer normal vector of $\Gamma^{coh}_{\triangle 0}$ and $\Gamma^{coh}_{\blacktriangle 0}$ respectively. By doing line integration along curves $\Gamma^{coh}_{\triangle 0}$ and $\Gamma^{coh}_{\blacktriangle 0}$, we can obtain the linear momentum conservation relation of cohesive zone (see Fig. 5):

$$\int_{\Gamma^{coh}_{\triangle 0}} \mathbf{N}_{\Gamma^{coh}_{\triangle 0}} \cdot \mathbf{P}_{\Gamma^{coh}_{\triangle 0}} d\Gamma + \int_{\Gamma^{coh}_{\blacktriangle 0}} \mathbf{N}_{\Gamma^{coh}_{\blacktriangle 0}} \cdot \mathbf{P}_{\Gamma^{coh}_{\blacktriangle 0}} d\Gamma = -l_0 h_0 \rho_0 \mathbf{b}_{coh} + l_0 h_0 \rho_0 \mathbf{a}. \tag{14}$$

The initial configuration of the cohesive zone is denoted by Ω_{coh0}. By invoking the Gaussian Theorem, the dynamic equilibrium relation of the cohesive zone is approximated as follow

$$\int_{\Omega_{coh0}} \mathrm{Div}(\mathbf{P}_{coh}) d\Omega + l_0 h_0 \rho_0 \mathbf{b}_{coh} = l_0 h_0 \rho_0 \mathbf{a}. \tag{15}$$

In computation, the aspect ratio $\varpi = h_0/l_0$ of cohesive zone is chosen around 10^{-3} to 10^{-5} in analogous to persistent slip bands. Practically, the bulk element partition of the domain of interests may be viewed as a mesoscale or macroscale finite element discretization at spatial scale l_0, without considering the virtual cohesive zones. In this case, the contribution of body force and inertia in cohesive zone can be lumped into corresponding bulk element nodes.

3.2 Galerkin variational formulation for EA-cohesive FEM

To solve a problem by using the EA-cohesive FEM in the frame of finite element method, we introduce the notion of the multiscale cohesive element discretization: given the domain Ω_0 of analysis, admit the existence of triangular sub domain $\Omega^e_{\triangle 0}$ in physical space, such that

$$\Omega_0 = \overline{\bigcup_e \Omega^e_{\triangle 0}}. \tag{16}$$

With the aid of trail function $\boldsymbol{u}^h$ and test function $\delta \boldsymbol{u}^h$, we obtain the following Galerkin Lagrangian weak formulation for the proposed cohesive finite element method

$$\sum_{e=1}^{n^{bulk}_{elem}} \left\{ \int_{\Omega^e_{\triangle 0}} (\rho_0 \ddot{\boldsymbol{u}}^h \cdot \delta \boldsymbol{u}^h + \mathbf{P}(\boldsymbol{u}) : \delta \mathbf{F}^h) d\Omega \right\} + \sum_{k=1}^{n^{coh}_{zone}} \left\{ \int_{\Omega^k_{coh0}} (\rho_0 \ddot{\boldsymbol{u}}^h \cdot \delta \boldsymbol{u}^h + \mathbf{P}_{coh}(\boldsymbol{u}) : \delta \overline{\mathbf{F}}^h) d\Omega \right\} = \sum_{e=1}^{n^{bulk}_{elem}} \left\{ \int_{\Omega^e_{\triangle 0}} \rho_0 \mathbf{b} \cdot \delta \boldsymbol{u} d\Omega + \int_{\partial_t \Omega^e_{\triangle 0}} \widetilde{\mathbf{T}} \cdot \delta \boldsymbol{u}^h d\Gamma \right\} + \sum_{k=1}^{n^{coh}_{zone}} \left\{ \int_{\Omega^k_{coh0}} \rho_0 \mathbf{b} \cdot \delta \boldsymbol{u} d\Omega + \int_{\partial_t \Omega^k_{coh0}} \widetilde{\mathbf{T}} \cdot \delta \boldsymbol{u}^h d\Gamma \right\} \tag{17}$$

where $\Omega^e_{\triangle 0}$, Ω^k_{coh0}, $\partial_t \Omega^e_{\triangle 0}$ and $\partial_t \Omega^k_{coh0}$ are the e-th element domain, the k-th cohesive zone domain, the natural boundary related to $\Omega^e_{\triangle 0}$ and the natural boundary of the k-th cohesive zone domain respectively. Even though the volume of the cohesive element ($\sim \varpi l_0^2$) is much smaller than the bulk element ($\sim l_0^2$), we still consider contributions due to inertia and body force inside cohesive zone. Since a cohesive zone shares the same FEM nodes with the adjacent bulk elements, inertia force and body force contributions are lumped to the corresponding FEM nodes. According to the linear momentum conservation of cohesive zone (see Eq. (14)), Eq. (17) can be simplified as follow,

$$\sum_{e=1}^{n^{bulk}_{elem}} \left\{ \int_{\Omega^e_{\triangle 0}} (\rho_0 \ddot{\boldsymbol{u}}^h \cdot \delta \boldsymbol{u}^h + \mathbf{P}(\boldsymbol{u}) : \delta \mathbf{F}^h) d\Omega \right\} + \sum_{k=1}^{n^{coh}_{zone}} \left\{ \int_{\Omega^k_{coh0}} \mathbf{P}_{coh}(\boldsymbol{u}) : \delta \overline{\mathbf{F}}^h d\Omega \right\} = \sum_{e=1}^{n^{bulk}_{elem}} \left\{ \int_{\Omega^e_{\triangle 0}} \rho_0 \mathbf{b} \cdot \delta \boldsymbol{u} d\Omega + \int_{\partial_t \Omega^e_{\triangle 0}} \widetilde{\mathbf{T}} \cdot \delta \boldsymbol{u}^h d\Gamma \right\} \tag{18}$$

By applying the divergence theorem to the cohesive zone Ω^k_{coh0}, the cohesive traction $\mathbf{T}_{coh}$ which is defined as $\mathbf{P}_{coh} \cdot \mathbf{N}_{coh}$ can be obtained:

$$\int_{\partial_t \Omega^k_{coh0}} \mathbf{T}_{coh}(\mathbf{u}) \cdot \delta \overline{\mathbf{u}}^h d\Gamma = \int_{\Omega^k_{coh0}} \mathbf{P}_{coh}(\mathbf{u}) : \delta \overline{\mathbf{F}}^h d\Omega, \tag{19}$$

where the $\mathbf{N}_{coh}$ is the outer normal vector of Ω^k_{coh0}. As we can tell from Eq. (19), the cohesive traction applies on the cohesive zone is a function of displacement filed of cohesive zone. Since we can evaluate the cohesive surface separation (normal separation and tangential separation) from displacement field $\mathbf{u}$, the we can obtain cohesive law for the proposed cohesive zone model with respect to $\mathbf{P}_{coh}$. It must be noted that the sign of the cohesive traction applying on cohesive zone is different with that of associated bulk element. For convenience, the union set of all natural boundary of cohesive zone is denoted as $\bigcup_k \partial_t \Omega^k_{coh0}$. By substituting Eq. (19) into Eq. (18), the final Galerkin weak formulation is obtained:

$$\sum_{e=1}^{n_{elem}^{bulk}} \left\{ \int_{\Omega_{\triangle 0}^{e}} (\rho_0 \ddot{\boldsymbol{u}}^h \cdot \delta \boldsymbol{u}^h + \mathbf{P}(\boldsymbol{u}) : \delta \mathbf{F}^h) d\Omega - \sum_{ek=1}^{n_e} \int_{\Omega_{coh0}^{ek} \bigcap (\bigcup_k \partial_t \Omega_{coh0}^k)} \mathbf{T}_{coh}(\boldsymbol{u}) \cdot \delta \overline{\mathbf{u}}^h d\Gamma \right\} = \sum_{e=1}^{n_{elem}^{bulk}} \left\{ \int_{\Omega_{\triangle 0}^{e}} \rho_0 \mathbf{b} \cdot \delta \boldsymbol{u} d\Omega + \int_{\partial_t \Omega_{\triangle 0}^{e}} \widetilde{\mathbf{T}} \cdot \delta \boldsymbol{u}^h d\Gamma \right\}, \tag{20}$$

where n_e is the number of adjacent cohesive zones of e-th bulk element $\Omega_{\triangle 0}^e$. For the consideration of efficiency, the lumped mass matrix is adopted. Then the cohesive traction contributed by the cohesive element can be lumped together via cohesive surface (boundary) integration and distributed to corresponding nodes. It is worthy emphasizing that the proposed cohesive zone model can simulate strong discontinuity without introducing displacement jump enrichment in the Galerkin weak formulation. In the proposed methodology, the cohesive law with respect to $\mathbf{P}_{coh}$ and bulk material response $\mathbf{P}$ are related to the microstructure and atomistic potential. In the following sections, an EHA constitutive model is developed based on embedded atom method. The EHA constitutive model provides a method based on first principle how to determine, from a macroscopic standpoint, whether a material point has entered softening deformation region or not.

Consider the following FE interpolation as the trial function $\mathbf{u}^h$ in each element

$$\mathbf{u}^h(\mathbf{X}) = \sum_{I=1}^{n_{node}} N_I(\mathbf{X}) \mathbf{d}_I, \tag{21}$$

where n_{node}, $N_I(\mathbf{X})$ and $\boldsymbol{d}_I$ are the node number of the element, shape function and nodal displacement of I-th node. Following the standard FE discretization procedure (e.g. [7]), the semi-discrete equation of motion is obtained:

$$\mathbf{M}\ddot{\mathbf{d}} + \mathbf{f}^{int}(\mathbf{d}) - \mathbf{f}^{coh}(\mathbf{d}) = \mathbf{f}^{ext} \tag{22}$$

where

$$\mathbf{M} = \mathop{A}_{e=1}^{n_{elem}} \int_{\Omega_{\triangle 0}^{e}} \rho_0 \mathbf{N}^{eT} \mathbf{N}^e d\Omega, \tag{23}$$

$$\mathbf{f}^{int} = \mathop{A}_{e=1}^{n_{elem}} \int_{\Omega_{\triangle 0}^{e}} \mathbf{B}^{eT} \mathbf{P}^e(\mathbf{d}) d\Omega, \tag{24}$$

$$\mathbf{f}^{coh} = \mathop{A}_{e=1}^{n_{elem}} \sum_{ek=1}^{n_e} \int_{\Omega_{coh0}^{ek} \bigcap (\bigcup_k \partial_t \Omega_{coh0}^k)} \mathbf{N}^{eT} \mathbf{T}_e^{coh} d\Gamma, \tag{25}$$

$$\mathbf{f}^{ext} = \mathop{A}_{e=1}^{n_{elem}} \left\{ \int_{\Omega_{\triangle 0}^{e}} \rho_0 \mathbf{N}^{eT} \mathbf{b}^e d\Omega + \int_{\partial_t \Omega_{\triangle 0}^{e}} \mathbf{N}^{eT} \widetilde{\mathbf{T}}^e d\Gamma \right\} \tag{26}$$

where $\boldsymbol{A}$, $\mathbf{N}^e$ and $\mathbf{B}^e$ are the element assemble operator, the element shape function matrix and the element B matrix respectively.

Explicit time integration algorithm is used to solve the discrete dynamic equations (see [7]). The brief flowchart for explicit time integration of the proposed cohesive finite element method is presented. After initializing the system, the force vectors can be computed. Then the acceleration of the present step can be obtained as:

$$\mathbf{a}_n = \mathbf{M}^{-1}\left(\mathbf{f}_n^{ext} - \mathbf{f}_n^{int} + \mathbf{f}_n^{cohe}\right). \tag{27}$$

Then the displacement field, acceleration field and velocity field can be updated respectively:

$$\mathbf{d}_{n+1} = \mathbf{d}_n + \mathbf{v}_n \Delta t_n + \frac{1}{2}\mathbf{a}_n \left(\Delta t_n\right)^2, \tag{28}$$

$$\mathbf{a}_{n+1} = \mathbf{M}^{-1}\left(\mathbf{f}^{ext} - \mathbf{f}^{int} + \mathbf{f}^{coh}\right), \tag{29}$$

$$\mathbf{v}_{n+1} = \mathbf{v}_n + \frac{1}{2}(\mathbf{a}_n + \mathbf{a}_{n+1})\Delta t_n, \tag{30}$$

where $\mathbf{d}_n$ is the displacement field at the time step at the time step n, $\mathbf{v}_n$ is the velocity field at the time step n, and $\mathbf{a}_n$ is the acceleration field at the time step n. The subscript n and $n+1$ denote to quantities evaluated at time t_n and t_{n+1}.

4 The embedded atom hyperelastic (EAH) constitutive model

In order to study material responses during fracture, more accurate and fundamental constitutive model is needed. In principle, crystalline defects, interatomic bonding, and many other properties can be studied by *ab initio* or first principle based calculations [18,20]. And the solution of multi-body Schrödinger equation can provide most accurate force field and displacement field at meso-scale [24]. However, due to the complexity of multi-body Schrödinger equations it is hard to solve mesoscale problem and almost impossible to solve macroscale (e.g. a micron to a millimeter) engineering problem by using *Ab initio* method with the current computer technology. Up to today, direct *ab initio* computations are only suitable for small systems of about a few thousand atoms with a median size supercomputer [29].

Instead of solving the Schrödinger equation of a many electron problem, one can approximate the system so that the total energy of a given atomic arrangement can be summed up over pair potentials [26]:

$$E_{total} = \frac{1}{2} \sum_{i,j(i \neq j)} \phi(r_{ij}). \tag{31}$$

If the pair potential is used, different atomistic bonds are independent. But this independency among atomistic bonds is a mis-representation of physical reality. Although the pair potential formalism has the advantage of computational simplicity, only in the case of noble gases can the interactions between atoms be described realistically by density-independent pair potentials. This limits the capacity and suitability of the pair potential in determining constitutive relations of solids and especially metallic materials. For instance, FCC metals usually have the ratio $C_{12} : C_{44}$ closer to 2 instead of 1 indicated by the Cauchy relation based on pairwise potentials simulations. This is because that the electrons of metallic material are not localized around the nuclei, and in fact, the valence electrons namely free-electron gas or electron glue are shared among ions. Pairwise potentials do not have enough capacity to simulate these properties. Daw and Baskes postulated that the energy in a crystal solid consists of the energy obtained by embedding an atom into a local electron density cloud. The local electron density cloud is determined by the surrounding atom configuration of the given atomic system [9,10]:

$$E_{total} = \sum_i E_i, \tag{32}$$

where E_i is the energy associated with ith atom. The E_i is given by:

$$E_i = F_\alpha \left(\sum_{j \neq i} \varrho_j(r_{ij}) \right) + \frac{1}{2} \sum_{i,j(i \neq j)} \phi(r_{ij}), \tag{33}$$

where F_α denotes the embedding function that represents the energy required to place i-th atom of type α into the background electron cloud, ϱ_j denotes the spherically averaged atomic electron density of the jth atom, and ϕ is the repulsive pair electrostatic interaction. Based on Eq. (33), in order to calculate atomic potential energy or elastic energy density, one needs to calculate the distance between each pair of two atoms. To do this, one has to carry out molecular dynamics computations.

However, if the local deformation is uniform, we may not need to use molecular dynamics to calculate stress as a quantity of assemble average, e.g. virial stress. Instead, we can use the Cauchy-Born rule, which only requires to calculate the stress in a single Wigner-Seitz cell. The application of the Cauchy-Born rule has two pre-requisites. The first pre-requisite is that the deformation of the underline lattice has to be uniform. When the first pre-requisite is satisfied, the spacial position of the atoms within the crystal lattice conform to the overall deformation of the medium. This situation can be expressed by the following simple mathematical expression:

$$\mathbf{r}_{ij} = \mathbf{F} \cdot \mathbf{R}_{ij}, \tag{34}$$

where $\mathbf{R}_{ij}$ is an undeformed lattice distance vector between the atom i and atom j, $\mathbf{r}_{ij}$ is the corresponding deformed lattice distance vector, and $\mathbf{F}$ is the uniform (constant) deformation gradient. The above expression basically implies that the distance between two arbitrary atoms is a function of deformation gradient, i.e. $|\mathbf{r}_{ij}| = f(\mathbf{F})$. The physical interpretation of such statement is that the mean displacement field uniquely determines the distance between two arbitrary atoms, and there is no displacement fluctuation when a region of a material undergoes uniform deformation. In the MCZM, we assume that the deformation inside each bulk element is uniform, therefore one can apply the Cauchy-Born rule to calculate the distance between two arbitrary atoms without invoking molecular dynamics calculations. Second, since the deformation is assumed to be homogeneous, so the stress state is also homogeneous; therefore one only needs to calculate stress at one (arbitrary) material point for an entire bulk element, and this stress should represent the stress state for the entire bulk element, whose size is at mesoscale. This is often done in practice by calculating the stress state at an arbitrary material point that is located in a supercell (see Fig. 6). For EAM calculation, the unit cell is not a conventional primitive cell but a much larger super-cell involving $3rd$ to $6th$ nearest neighbors of the center atom. Let us denote the position of the center atom in the super-cell as $\mathbf{X}_i$ in the referential configuration, and $\mathbf{x}_i$ in the current configuration, then the referential bond vector between i-th and j-th atom is given by:

$$\mathbf{R}_{ij} = \mathbf{X}_j - \mathbf{X}_i. \tag{35}$$

By applying the affine mapping $\mathbf{F}$ on those referential bond vectors, the deformed bond vectors between the i-th and j-th atom is given by

$$\mathbf{r}_{ij} = \mathbf{x}_j - \mathbf{x}_i = \mathbf{F}\mathbf{R}_{ij}, \quad i \neq j, \quad i, j = 1, 2, \ldots, n_{atom} \tag{36}$$

where n_{atom} is the total number of atoms within the given atomic super-cell associated to the domain undergoing the deformation.

Based on the assumption of homogeneous deformation in the bulk element and the EAM formalism, the elastic energy density in the bulk material an be derived from the potential energy density in a lattice unit cell. The elastic stored energy function W_e is given by:

$$W_e = \frac{1}{V_t} \sum_i^{n_{atom}} E_i = \frac{1}{J V_0} \sum_i^{n_{atom}} E_i, \tag{37}$$

where J is the Jacobian defined as $det(\mathbf{F})$, E_i is the energy of a single atom defined in the embedded atom model (see Eq. (33)), and V_t and V_0 are the volumes of the deformed

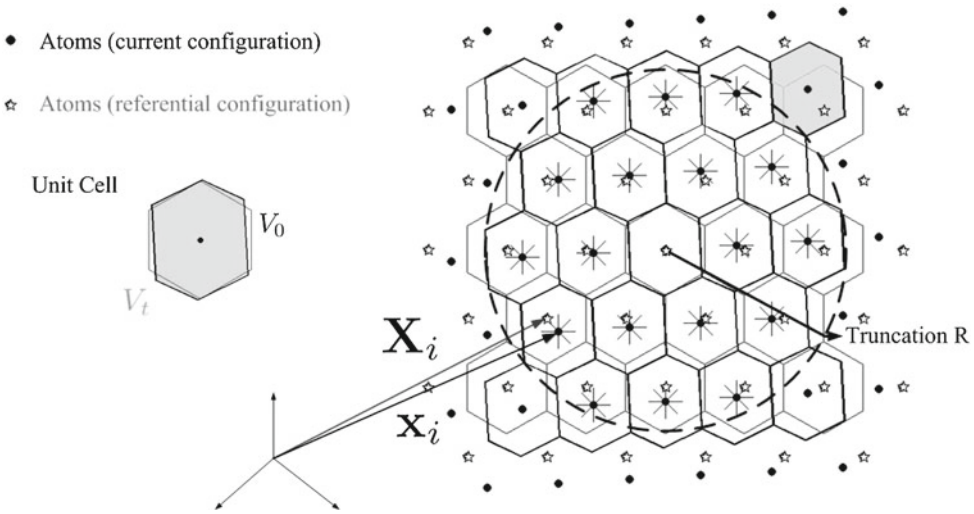

Fig. 6 Depiction of super-cell and conventional unitcell with respect to the reference configuration and deformed configuration

and undeformed configuration respectively (as depicted in Fig. 6). In particular, it should be noted that the surface mapping in 2D problem should invoke the conjugate of deformation gradient. Since E_i is a function of current bond vectors $\mathbf{r}_{ij}$ defined on the current configuration, if we assume that the deformation in a local region is uniform, the total energy becomes a function of deformation gradient $\mathbf{F}$. Then the elastic energy density W_e is given as,

$$W_e(\mathbf{F}) = \frac{1}{det(\mathbf{F})V_0}\sum_{i}^{n_{atom}} E_i(\mathbf{F}) = \widetilde{W}_e(\mathbf{E}) \tag{38}$$

where $\mathbf{E} = \frac{1}{2}(\mathbf{C} - \mathbf{I})$ is the Green-Lagrangian strain tensor.

Since the energy change within the embedded atom model is independent of the loading path, which implies the existence of the stored elastic energy function, and it then leads to the the constitutive relation for the bulk material at mesoscale:

$$\mathbf{S} = 2\frac{\partial\psi(\mathbf{C})}{\partial\mathbf{C}} = \frac{\partial\widetilde{W}_e(\mathbf{E})}{\partial\mathbf{E}} \tag{39}$$

where $\mathbf{S}$ is the $2nd$ Piola Kirchhoff stress (PK-II), $\mathbf{C}$ is the right Green Deformation tensor and ψ is the store energy function with respect to $\mathbf{C}$. By substituting the $\widetilde{W}_e(\mathbf{E})$, an EAH constitutive model in terms of the PK-II stress tensor with respect to $\mathbf{E}$ at the position of the ith atom is given by:

$$\mathbf{S}_i = \frac{1}{det(\mathbf{F})V_0}\left\{\frac{1}{2}\sum_{j\neq i}\phi'(r_{ij})\frac{\mathbf{R}_{ij}\otimes\mathbf{R}_{ij}}{r_{ij}} + F'_\alpha(\vartheta_i)\sum_{j\neq i}\varrho'_j(r_{ij})\frac{\mathbf{R}_{ij}\otimes\mathbf{R}_{ij}}{r_{ij}}\right\}, \tag{40}$$

where $\vartheta_i = \sum_{j\neq i}\varrho'_j(r_{ij})$ is the electron density at the position of i-th atom in the background electron cloud. Although the 2nd Piola–Kirchhoff stress is convenient in constructing the constitutive model, it results in a cumbersome expression in the balance equation of linear momentum, whereas the 1st Piola–Kirchhoff stress (PK-I) works better. Alternatively, the EAH constitutive model expressed in the form of PK-I stress tensor $\mathbf{P}_i$ is also given as follows,

$$\mathbf{P}_i = \frac{1}{det(\mathbf{F})V_0}\left\{\frac{1}{2}\sum_{j\neq i}\phi'(r_{ij})\frac{\mathbf{r}_{ij}\otimes\mathbf{R}_{ij}}{r_{ij}} + F'_\alpha(\vartheta_i)\sum_{j\neq i}\varrho'_j(r_{ij})\frac{\mathbf{r}_{ij}\otimes\mathbf{R}_{ij}}{r_{ij}}\right\}. \tag{41}$$

According to the derived EAH constitutive model, it is possible to link atomistic scale information with constitutive response on higher scale level. Since fracture is intrinsically a multiscale phenomenon, the multiscale EAH finite element approach may provide some advantages in simulation of fracture.

5 Behaviors of EAH material in bulk element and cohesive zone

Now the most crucial problem is how to calculate the stress based on the derived EAH constitutive formalism. As a coarse-graining constitutive model, EAH bridges the atomistic scale and the mesoscale or even macroscale. It is a method to determine material behavior from a macroscopic standpoint based on first principle. From a mathematical standpoint, the EAH also provides a more complete constitutive formalism. As an atomistic potential formalism, EAM is based on the density functional theory (DFT), and the reliability is guaranteed by fitting the atomistic potential functional to the *ab initio* or first principle results [25,30]. Likewise, by carefully fitting EAH parameters with the experimental and

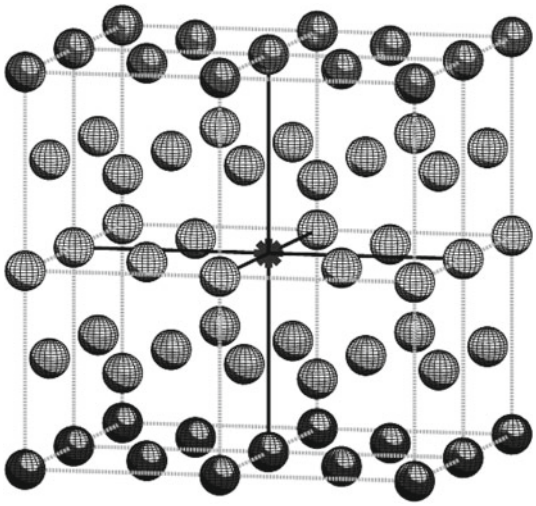

Fig. 7 The $2 \times 2 \times 2$ fcc super-cell for calculating the background free electron gas

first principle calculation data, the EAH constitutive model may work for a host of metallic materials.

In EAM theory, the background electron density ϑ_i is the density at the reference atom site (i.e. i-th atom of interest) due to the host atoms [4], i.e. the surrounding atoms in the lattice. Unlike the pairwise potential, the EAM is a multibody potential in principle. Then a super-cell is needed to perform the calculation on the background electron density within a plane-wave periodic framework [9,11]. As illustrated in Fig. 7, the super-cell is constructed by stacking a couple of conventional unit cells together without the atom in question in the center. For example, the supercell shown in Fig. 7 can be denoted as a $2 \times 2 \times 2$ super-cell. The super-cell consists of eight primitive unit cells.

For demonstration purpose, we select metal Cu as a simple illustration. The atomic electron density function for Cu is given by:

$$\varrho(r_{ij}) = \varrho_e \exp\left(A - \frac{A r_{ij}}{r_{1e}}\right), \tag{42}$$

where r_{1e} denotes the distance to the $1st$ nearest neighbor atom in lattice at equilibrium state and ϱ_e and A are given as 2.114 nm^{-3} and 6.47 respectively for copper. Given an arbitrary ith atom, then the electron density ϑ_i (defined in Eq. (40)) at the position of i-th atom can be calculated based on different super-cells. The calculated background electron densities for different sizes of super-cells are compared with the reference value in Table 1. The differences between the calculated background electron gas and the reference value for Cu are all less than 1%. In general, the EAM potential has two generic parts: the part coming from local electron density, and a pair potential part. The Coulomb potential or Coulombic type potentials are the most commonly used as pair potential in EAM. The general form of the Coulombic type pairwise term is given as follows [14],

$$\phi_{\alpha\beta}(r_{ij}) = \frac{Z_\alpha(r_{ij}) Z_\beta(r_{ij})}{r_{ij}}, \tag{43}$$

where α and β denote the types of atoms, Z_α and Z_β denote the effective charges of respective atoms. It has been shown that it is possible to obtain effective charges $Z(r_{ij})$ to accurately describe the energy of system. Such a pairwise potential definitely decreases monotonically with the increasing separation [11,14,41]. By assuming functional forms for $Z(r_{ij})$, the parameters in EAM can be adjusted to fit know bulk properties (e.g. lattice constants, elastic constants etc.) and many specific functional forms can come out. For convenience, an analytic form of pairwise potential for Cu is given by

$$\phi(r_{ij}) = -\phi_e\left(1 + C\left(\frac{r_{ij}}{r_{1e}} - 1\right)\right)\exp\left(-D\left(\frac{r_{ij}}{r_{1e}} - 1\right)\right), \tag{44}$$

where the parameters C, ϕ_e and D are given as 12.06, 0.1217 eV and 6.82054 respectively.

Traditional embedding functions F_α with respect to atoms α from H to Ar are parameterized within the frame of homogeneous electron gas based on a DFT-type formalism (e.g. [34,35,41]). Due to the heterogeneity of the electron gas in the neighborhood of the atom in question, this universal functional form of the embedding function can be written as follows:

$$F_\alpha(\vartheta_i) = F_0\left(1 - h\ln\left(\frac{\vartheta_i}{\vartheta_e}\right)\right)\left(\frac{\vartheta_i}{\vartheta_e}\right)^h, \tag{45}$$

where F_α represents the parametrization of embedding energy function of α atom, and F_0 is the model fitting parameters related to model fitting parameter h and Cauchy discrepancy. The ϑ_e is the background electron gas density, which is calculated and tabulated in Table 1 for Cu. Figures 8 and 9 illustrate the embedding energy dependence on the electron density and interatomic distance that are expressed in Eqs. (42) and (45). The model fitting parameter h is chosen as 0.55, and the embedded energy model fitting parameter F_0 is chosen as -2.19 for parametrization. Due to the differences of the calculated electron densities, there are deviations in the embedding energy calculation, which however is less than 10^{-3}eV. On the other hand, differences between experimental values of the embedding energy range from 10^{-3} to 10^{-1} eV [41], which is mainly due to spatial fluctuation of electron density. Within such range, the fluctuation in the calculated values of embedding energy due to the size of the super-cell may also be tolerated.

With the concern of energy conservation and computational efficiency, the following cutoff function [5] can be implemented in the atomic electron density calculation, and the parameter of related potential function are as follows:

Table 1 The calculated background free electron gas densities on different super-cells

	Super-cell	Atom No.[a]	ϑ_{ie} (Å^{-3})	Difference (%)
Cu	$2 \times 2 \times 2$	32	2.650000e−002[b]	0.0000000000000000
	$2 \times 2 \times 2$	32	2.67233958e−002	0.8430030188679303
	$4 \times 4 \times 4$	256	2.67432150e−002	0.9177924528301943
	$6 \times 6 \times 6$	864	2.67432185e−002	0.9178056603773572

[a] Including the atom in question
[b] Reference given by [41]

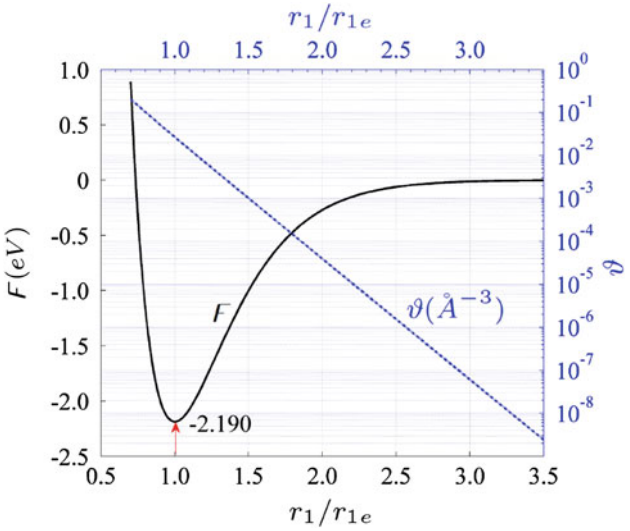

Fig. 8 The calculated embedding energy F(eV) and the calculated background electron density ϑ(Å^{-3}) of Cu versus the dimensionless atomistic distance r_1/r_{1e}

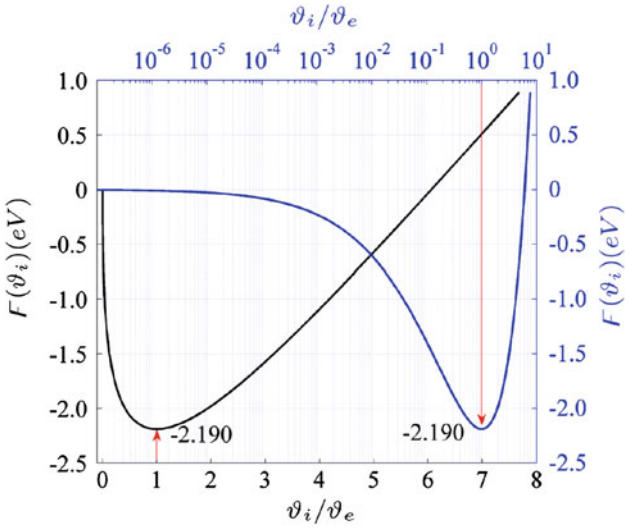

Fig. 9 Embedding energy $F(\vartheta_i)$ (eV) versus the dimensionless electron density ϑ_i/ϑ_e

$$f(r_{ij}) = \begin{cases} 1, & \breve{r} \in [1, \infty) \\ \left(1 - (1 - \breve{r})^4\right)^2, & \breve{r} \in [0, 1] \\ 0, & \breve{r} \in (-\infty, 0] \end{cases} \tag{46}$$

where $\breve{r} = (r_c - r_{ij})/\delta_r$ is the dimensionless distance, and the smoothing cutoff region δ_r can be taken as 0.1 Å specially for Cu.

As illustrated in Fig. 9, the embedding energy goes to zero, when the electron density ϑ approaches zero.

5.1 EAH constitutive model in bulk region

In the proposed EAH constitutive model, the EAM potentials are implemented to offer atomistic information and construct coarse-graining material response on mesoscale or even macroscale. In Fig. 10a, we show an EAH constitutive model with parameters obtained from an EAM calculation for single crystal Cu. In this case, a type of (hydrostatic stress $tr(\mathbf{S})/3$) tri-axial loading is applied to a specimen by prescribed uniformed strain loading $E_{11} = E_{22} = E_{33}$. It can be see from Fig. 10a that the EAH material is able to sustain infinitely large hydrostatic compression. On the other hand, it shows that the stress-strain relation can capture the strain softening phenomena naturally. When the stress level exceeds a critical value the post-peak behavior or post-yielding behavior of single crystal Cu becomes unstable, and the material state in that part of stress-strain relation may be viewed as the failure state in engineering. As illustrated in Fig. 10a, a single crystal Cu will fail due to the atomistic debonding. Juxtaposing with the hydrostatic stress and hydrostatic strain, we also plot the relationship between the the isotropic volume strain $\varepsilon_V = J - 1$. It can also be approximated by the trace of the Green-Lagrangian strain tensor i.e. E_{ii} when the strain is small. From Fig. 10a, one can see that a single crystal Cu is failing when the volumetric strain is actually increasing. Physically, as the distance between two atom increases, the strength of the interatomic bond becomes weaker and weaker such that the atoms will not stay together anymore. In Fig. 10b, the mesoscale constitutive relation obtained under a constrained uniaxial tension and compression is depicted $E_{11} \neq 0$ and $E_{22} = E_{33} = 0$. As the uniaxial strain E_{11} increases from the stress free state, the tensile stress component S_{11} with respect to the straining increases until the critical cohesive state. Due to the strain-constraint conditions ($E_{22} = E_{33} = 0$), the

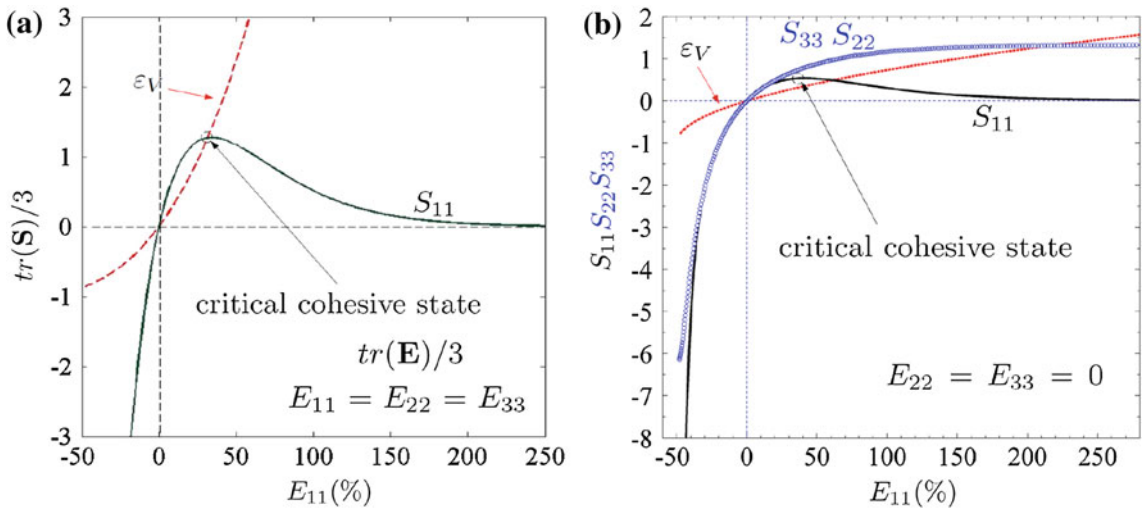

Fig. 10 The behavior of EAH (embedded atom hyperelastic) constitutive model in bulk region (Cu). **a** Hydrostatic stress $tr(\mathbf{S})/3 = S_{11} = S_{22} = S_{33}$ of EAH material in bulk element with respect to triaxial loading ($E_{11} = E_{22} = E_{33} = tr(\mathbf{E})/3$). **b** Components of PK-II S_{11}, S_{22}, S_{33} of EAH material in bulk region vs. constrained uniaxial loading ($E_{11} \neq 0$, $E_{22} = E_{33} = 0$)

volumetric strain is only a function of the line strain E_{11}. As observed from Fig. 10b, all the normal stress components S_{22}, S_{33} are non-zero, which is the manifestation of the Poisson's ratio effect, and it indicates that the deformed atomistic configuration is not the lowest energy state under the prescribed deformation constraint. In order to attain a minimum state, lattice structure will develop lateral deformation. Otherwise lateral stress will develop to manifest the corresponding deformation tendency when the lateral deformation is constrained.

5.2 EAH material in cohesive zone and EAH cohesive law

The interface between the bulk regions is described by cohesive zones in EA-cohesive FEM, for which the associated EAH cohesive law is proposed. The most frequently adopted cohesive law in literature should be the exponential, or sinusoidal, type of cohesive laws [40], which made a great success in describing the work-of-separation under mode-I, mode-II even mixed-mode conditions. For the EA-cohesive FEM proposed here, evidently an adequate cohesive law of relevant loading conditions is required to predict the occurrence of delamination and crack propagation etc. in engineering structures. Based on EAM, the associated EAH cohesive law can be naturally derived by invoking the Cauchy-Born rule. In EA-cohesive FEM, all defects and damage are assumed to be confined within the cohesive element, which is essentially a finite width interface. Hence, its behavior may be characterized by the cohesive constitutive relations in terms of the normal and tangential separation.

In EAH cohesive law, the energy of separation of cohesive zone with respect to normalized normal opening is depicted

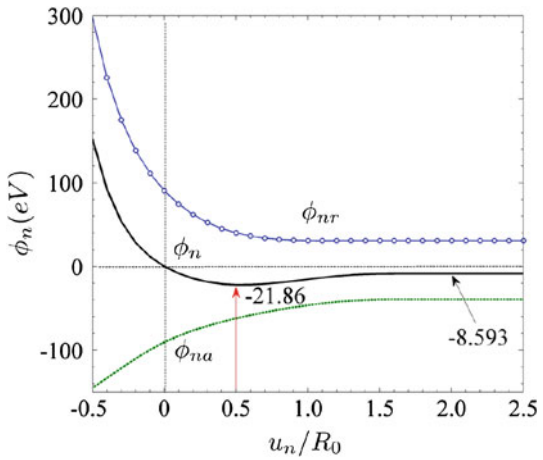

Fig. 11 The normal EAH cohesive energy ϕ_n and its repulsive part and attractive part with respect to the pure normal separation u_n/R_0 when the EAH cohesive zone is under mode-I loading condition

in Fig. 11, where the dimensionless normalized normal separation is given as u_n/R_0 and the energy of separation is given as ϕ_n. u_n is the normal separation, and R_0 is the balance distance between the nearest neighbor atoms in the given super-cell, which is material-dependent. The normal cohesive energy of separation ϕ_n can be decomposed into two parts as repulsive cohesive energy of separation ϕ_{nr} and attractive cohesive energy of separation ϕ_{na}. As depicted in Fig. 11, the energy of cohesive zone with respect to repulsive interaction (the pairwise term in EAM) drops quickly as the dimensionless normal opening increases in analogy to the atomistic repulsive force. Also, the attractive energy of cohesive zone increases as the dimensionless u_n/R_0 increases.

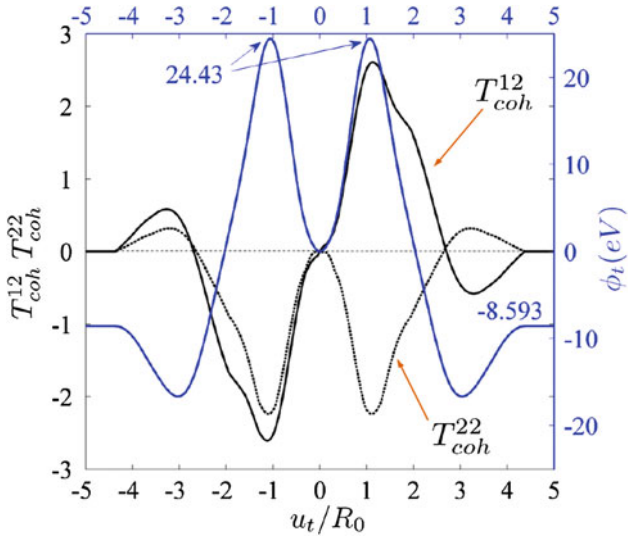

Fig. 12 The tangential EAH cohesive energy ϕ_t, tangential cohesive traction T^{12}_{coh}, and normal cohesive traction T^{22}_{coh} versus tangential separation u_t/R_0

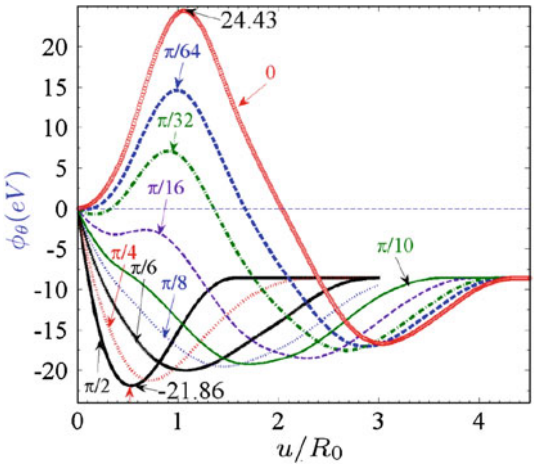

Fig. 13 Cohesive energy in mixed-mode with respect to the tangential separation u/R_0 under different loading angles θ

Evidently, the total cohesive energy of separation is the direct superposition of the repulsive and attractive cohesive energies. The characteristic of the cohesive energy of separation is the same with energy of separation of other proposed cohesive laws in literature. The existence of energy well which is also originated from the EAM potential justifies the proposed model as a cohesive law.

The responses with respect to tangential separation (tangential cohesive energy ϕ_t, tangential cohesive traction T^{12}_{coh} and normal cohesive traction T^{22}_{coh}) are shown in Fig. 12. As can be seen, the shear traction (denoted as T^{12}_{coh}), increases as the tangential separation u_t/R_0 increases until the critical cohesive length (approximately $1.2R_0$). When the tangential displacement is beyond the characteristic length, the shear traction decreases and vanishes at around $4.2R_0$, leading to complete shear failure. To interpret the result, we first zoom into the atomistic scale. At atomistic scale, the atoms locates in its equilibrium position with lowest energy. When the sliding between two adjacent atomic plane initializes, the atoms would move to higher energy state by overcoming associated resistance. The resistance has a peak and after reaching the peak, it will drop. For the lattice of perfect crystal, such atomistic resistance is periodic. However, due to the presence of defects such as, dislocation, grain boundary, twin boundary, etc. the lattice periodicity at mesoscale does not exist for most engineering materials. The vanishing of shear cohesive (Fig. 12) traction demonstrates this point. In Fig. 12, the tangential energy of separation ϕ_t is plotted, in which ϕ_t increases as the tangential separation increases, and it starts to decrease after reaching the peak point of tangential traction and finally approaches to a constant. To investigate the coupling between the normal cohesive traction (T^{22}_{coh}) and the tangential separation, the tendency of the changing with respect to normal cohesive traction during pure tangential separation is also plotted in Fig. 12. Likewise, the normal cohesive traction that increases at the beginning of the tangential separation and deceases when beyond approximately $1.0R_0$, is mostly attractive except in the tail of interaction.

The combined influence of normal and tangential separation under mixed-mode loading with constant separation angle θ is shown in Fig. 13 in terms of coupled cohesive energy of ϕ_θ. As can be seen from the figure, when the $\theta = 0$ it stands for the cohesive energy under purely tangential separation (ϕ_t) and likewise when $\theta = \pi/2$ it stands for the cohesive energy under the purely normal separation (ϕ_n). To demonstrate the capacity of the EAH model to describe mixed mode cohesive law, the mixed-mode cohesive energy, ϕ_θ under different loading angle θ, are calculated.

The influence of the loading angle θ on the cohesive energy ϕ_θ is illustrated by smooth transition as θ changes continuously. No coupling parameters are needed in constructing the mixed-mode cohesive relation. The reason for the natural coupling for mixed mode is that the normal as well as the tangential cohesive traction is derived from EAH constitutive model in the cohesive zone.

6 Numerical examples

In this section, numerical examples are presented to demonstrate the capability of the EA-cohesive FEM and EAH constitutive model.

6.1 Case I: validation of EA-cohesive FEM and EAH

Molecular dynamics (MD) is a natural and powerful method that can be use to simulate fracture at atomistic scale. When

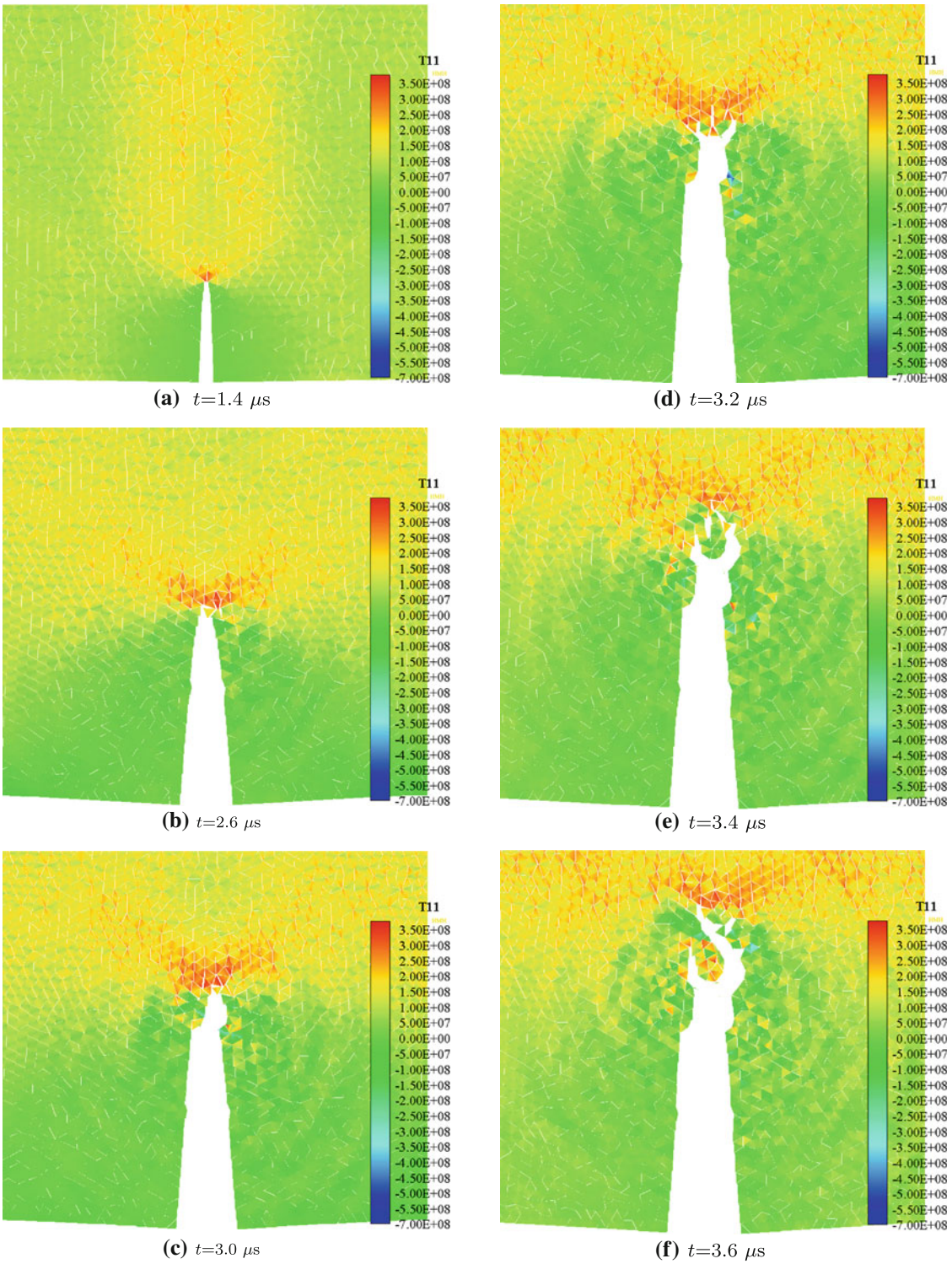

Fig. 14 Evolution of the crack tip field

spatial scale and temporal scale increase, one may need to use massively parallel MD to carry out the fracture simulation to overcome the computation cost. To validate the multiscale EA-cohesive FEM, we carry out a comparison study between the multiscale EA-cohesive FEM and MD paradigm. A large scale MD simulation of fracture using EAM potential is chosen from literature [19]. The same analytical EAM potential is implemented to construct the associated EAH constitu-

tive model and EA-cohesive FEM model. The same mode-I tensile loading is also applied to the EAH specimen in our EA-cohesive FEM. To compare with the MD simulation, the same parameters are used in constructing the EAH specimen. One may note that the time duration of the simulation is limited by the traversal time period of the acoustic wave emitted from the crack tip and bounced back from the traction-free boundary, which may cause additional reflection wave loading at the crack tip and complicate the physical phenomenon.

In order to compare with the results of MD simulation, the exact same problem set-up is considered. The precracked specimen is governed by the proposed EAH constitutive relation with the same EAM parameters. The EAH specimen in the EA-cohesive FEM model is composed of 12,894 bulk elements and 19,171 cohesive elements while the reported MD simulation used 300,000–600,000 atoms. As the crack propagates, the acoustic waves that have been emitted from the crack tip will return back to the newly born crack region by the reflection from the free boundaries of the EA-cohesive model. As illustrated in Fig. 14, the acoustic wave perturbs the propagation of the crack, and it may cause the crack bifurcation. Similar with large scale MD simulation results, the acoustic waves emitted from the crack opening due to crack generation (bond breakage) have already bounced off the top free surface and appear as a family of concave upward arcs that intersect concave downward arcs from later bond-breaking events. According to the discussions in the literature, without proper acoustic wave absorption mechanism at the boundary of the specimen, the reflection of the elastic waves would set up a time limit ($T_{limit} = L_x/c$) for unperturbed crack propagation. The crack velocity versus time for EAM crystal calculated by large scale MD simulation is reported. The crack propagation velocity history computed by EA-cohesive FEM is compared with that of the large scale MD simulation in Fig. 15. Time unit is $20t_0$ [19]. According to the simulation, the initiation time of crack propagation of EA-cohesive model is a little earlier than that of large scale MD. However the peak velocity of the EA-cohesive FEM is 93.6% the peak velocity measured by large scale MD. Besides the original path of the crack, the velocity of new path of the forked crack is also illustrated in Fig. 15. Constant stain rate ($\dot{\varepsilon} = 8 \times 10^{-7}$) is applied during the whole loading period in the EA-cohesive FEM simulation. The Newmark-β integration scheme and the central difference integration method are both been used in the simulation, and the time step is chosen as $\Delta t = 0.20 \times 10^{-012}$s. As can be seen, the EA-cohesive FEM with 12,894 elements can get satisfactory simulation in comparison with the large scale MD with 300,000 atoms involved, which makes the proposed EA-cohesive FEM more computationally economic than that of MD simulation and hence it is more suitable for mesoscale or even macroscale fracture simulations.

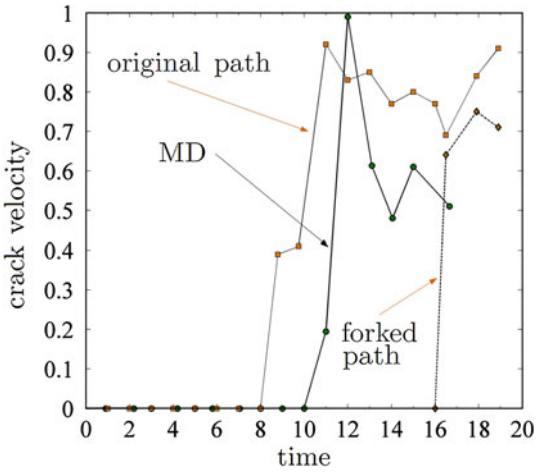

Fig. 15 Comparison of crack velocity histories obtained from simulations the results of large scale MD and EA-cohesive FEM

6.2 Case II: fracture simulation of a Cu foil

The second example is a simulation of fracture of a copper foil with the dimension (3 mm × 2 mm) (see Fig. 16). In this simulation, the copper foil specimen is subjected to a dynamically prescribed symmetric uniaxial tension load in x-axis direction. During the entire simulation, a constant time step is chosen as $\Delta t = 1 \times 10^{-11}$s for time integration. The crack growth and propagation are successfully observed during the simulation. There are two small pre-cracks at the upper edge and the lower edge, which are rotational symmetrically located. The simulation shows that during the loading process the two crack tips attract each other, and eventually the two cracks merge dynamically to form one single through-crack. The whole specimen consists of 1,354 bulk elements and 1,979 cohesive zones. At such spatial scale, take a typical foil thickness $10\mu m$ as example, there are almost millions of trillions atoms (10^{18}) in the specimen, and it is impossible to use MD to simulate fracture by using today's computer technology. However, by using the proposed EA-cohesive FEM, we are able to carry out fracture simulation at macroscale with some atomistic features.

7 Conclusions

The theory and computational algorithm of an EA-cohesive FEM and the associated embedded atom hyperelastic (EAH) constitutive model have been presented in this paper. It is shown that in comparison with the pair potential based multiscale cohesive zone model implementing EAM potentials in a cohesive FEM achieve accuracy and fidelity in material modeling and simulation of fracture. From the perspective from atomistic scale, the essence of fracture is interatomic interactions. Besides *ab initio* method, EAM is an alternative

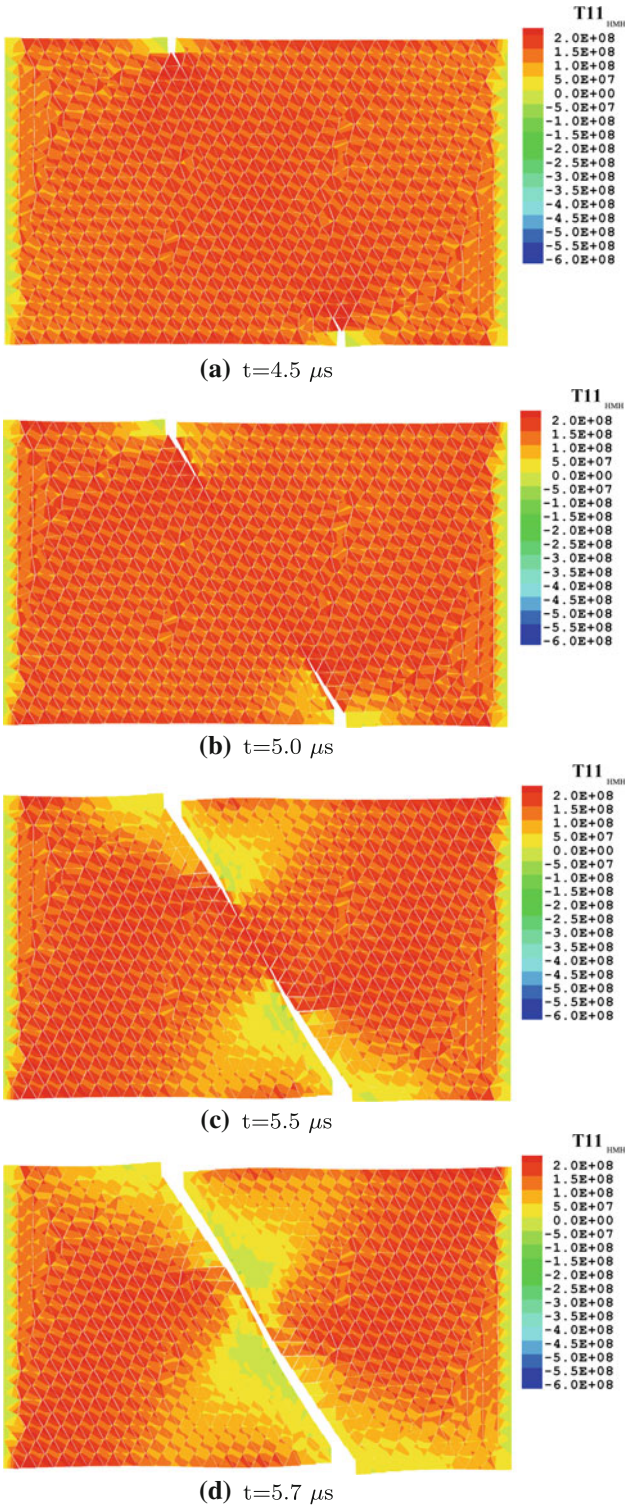

Fig. 16 The prototype crack propagation simulation of Cu foil with precracks based on EA-cohesive FEM and EAH

formalisms for describing realistic interatomic behavior with computational efficiency. In the proposed EA-cohesive FEM, the material domain of the interest is discretized by a set of bulk elements and cohesive elements that are assigned with certain certain microstructure to enable atomistic informed mesoscale constitutive relation. Within the bulk element, the material can be viewed as a Cauchy continuum so that the formulae of continuum mechanics may be applied. Within the cohesive interphase, the cohesive law can be developed with the aid of the EAH constitutive model. Compared to conventional cohesive zone model, the EA-cohesive FEM builds its cohesive relation by taking into account material micro-structure, local electron density, and atomistic bonding condition, it is an approach that is fundamental superior than the approach of empirical cohesive law. Compared with the previous pairwise-potential-based cohesive zone method [43], the weakness of the pairwise potential has been overcome by adopting EAM formalism, and additional hour-glass control measure is taken to fix the drawback of the overly simplified effective deformation gradient map. It has been shown that the proposed EA-cohesive FEM and EAH constitutive can simulate crack growth problems for engineering materials at mesoscale or macroscale. Since the EAH constitutive model is enriched by lattice and atomistic information, the proposed EAM cohesive finite model will be suitable for solving small scale problems. On the other hand, it may also work for macroscale problems of engineering material.

As a validation of the EA-cohesive FEM, we have carried out a simulation of crack propagation in single crystal Cu foil, which can be extend to simulating small scale fractures of other materials with different lattice structures. However, considering that the EAM is originally built for metallic material systems by taking into account the contribution of the free electron density [9], the EA-cohesive finite element method may be only applied to the metallic material systems in order to gain a satisfactory accuracy and to utilize abundant reference databases. It should be noted that the derivation of the EAM-based multiscale cohesive constitutive formulae is based on the universal formalism of EAM, hence any well fitted EAM potentials can be implemented in multiscale finite element computations. We believe that by fitting the multiscale EAH constitutive formalism with the experimental and first principle database, the EAH constitutive formalism may provide a viable simulation tool for a wider range of materials. As a multiscale constitutive model, EAH bridges the atomistic scale and the mesoscale or even macroscale. It is a method to determine material behavior from a macroscopic standpoint based on first principle. From a mathematical standpoint, the EAH also provides a more flexible constitutive formalism. It should be emphasized that the derivation of the EAH constitutive formulae is general, which is valid for any EAM formulae. Owing to the independency of the derived formulae, any well fitted EAM potentials can be implemented in the formulae for specific simulation need. As an atomistic potential formalism, EAM is based on the density functional theory (DFT), and its reliability is

guaranteed by fitting the atomistic potential functional to the *Ab initio* or first principle results [25,30]. Likewise, by further fitting the multiscale EAH constitutive formalism to the experimental and first principle database, the EAH constitutive formalism is promising in better simulating a wider material range.

Acknowledgments The authors gratefully appreciate the support from National Natural Science Foundation of China (NSFC Grant 50878117, NSFC Key Project Grant 51038006), China Scholarship Council Project (M.H. HE-2009621076) and a grant from NSF (Grant No. CMMI-0800744)(SL).

References

1. Adams JB, Foiles SM (1990) Development of an embedded-atom potential for a bcc metal: vanadium. Phys Rev B 41(6):3316–3328
2. Barenblatt GI (1959) The formation of equilibrium cracks during brittle fracture: general ideas and hypothesis, axially symmetric cracks. Appl Math Mech (PMM) 23:622–636
3. Borst Rd, Gutirrez MA, Wells GN, Remmers JJC, Askes H (2004) Cohesive-zone models, higher-order continuum theories and reliability methods for computational failure analysis. Int J Numer Methods Eng 60(1):289–315
4. Baskes MI (1992) Modified embedded-atom potentials for cubic materials and impurities. Phys Rev B 46(5):2727–2742
5. Baskes MI (1997) Determination of modified embedded atom method parameters for nickel. Mater Chem Phys 50(2):152–158
6. Braides A, Lew AJ, Ortiz M (2006) Effective cohesive behavior of layers of interatomic planes. Arch Ration Mech Anal 180:151–182
7. Belytschko T, Liu WK, Moran B (2000) Nonlinear finite elements for continua and structures. Wiley, Chichester
8. Cao N, Chen S, Jin S, Mart D (1997) Physical symmetry and lattice symmetry in the lattice Boltzmann method. Phys Rev E 55(1):R21–R24
9. Daw MS, Baskes MI (1983) Semiempirical, quantum mechanical calculation of hydrogen embrittlement in metals. Phys Rev Lett 50(17):1285–1288
10. Daw MS, Baskes MI (1984) Embedded-atom method: derivation and application to impurities, surfaces, and other defects in metals. Phys Rev B 29(12):6443–6453
11. Daw MS, Foiles SM, Baskes MI (1993) The embedded-atom method: a review of theory and applications. Mater Sci Reports 9(7–8):251–310
12. Ewing JA, Walter R (1900) The crystalline structure of metals. Philos Trans R Soc Lond A 195:279–301
13. Ericksen JL (2008) On the Cauchy-Born rule. Math Mech Solids 13(3–4):199–220
14. Foiles SM, Baskes MI, Daw MS (1986) Embedded-atom-method functions for the fcc metals Cu, Ag, Au, Ni, Pd, Pt, and their alloys. Phys Rev B 33(12):7983–7991
15. Geubelle PH, Kulkarni MG, Matous K (2010) Coupled multi-scale cohesive modeling of failure in heterogeneous adhesives. Int J Numer Methods Eng 84:916–946
16. Gao H, Klein P (1998) Numerical simulation of crack growth in an isotropic solid with randomized internal cohesive bonds. J Mech Phys Solids 46(2):187–218
17. Hayes RL, Ortiz M, Carter EA (2004) Universal binding-energy relation for crystals that accounts for surface relaxation. Phys Rev B 69:172104
18. Hagen G, Papenbrock T, Hjorth-Jensen M (2010) Ab initio computation of the ^{17}f proton halo state and resonances in $a = 17$ nuclei. Phys Rev Lett 104(18):182501
19. Holian BL, Ravelo R (1995) Fracture simulations using large-scale molecular dynamics. Phys Rev B 51(17):11275–11288
20. Hong T, Freeman AJ (1991) Effect of antiphase boundaries on the electronic structure and bonding character of intermetallic systems: Nial. Phys Rev B 43(8):6446–6458
21. Jones JE (1924) On the determination of molecular fields. I: from the variation of the viscosity of a gas with temperature. Proc R Soc Lond Ser A 106(738):441–462
22. Jones JE (1924) On the determination of molecular fields. II: from the equation of state of a gas. Proc R Soc Lond A 106(738):463–477
23. Johnson RA, Oh DJ (1989) Analytic embedded atom method model for bcc metals. J Mater Res 4:1195–1201
24. Jensen F (2006) Introduction to computational chemistry. Wiley, New York
25. Johnson RA (1988) Analytic nearest-neighbor model for fcc metals. Phys Rev B 37(8):3924–3931
26. Kaxiras E (2003) Atomic and electronic structure of solids. Cambridge University Press, Cambridge
27. Klein P, Gao H (1998) Crack nucleation and growth as strain localization in a virtual-bond continuum. Eng Fract Mech 61:21–48
28. Liu X., Li S., Sheng N. (2008) A cohesive finite element for quasi-continua. Comput Mech 42:543–553
29. Mishin Y, Mehl MJ, Papaconstantopoulos DA (2002) Embedded-atom potential for $B2$-$N_i Al$. Phys Rev B 65(22):224114
30. Mei J, Davenport JW, Fernando GW (1991) Analytic embedded-atom potentials for fcc metals: application to liquid and solid copper. Phys Rev B 43(6):4653–4658
31. Moes N, Dolbow J, Belytschko T (1999) A finite element method for crack growth without remeshing. Int J Numer Methods Eng 46(1):131–150
32. Nguyen O, Ortiz M (2002) Coarse-graining and renormalization of atomistic binding relations and universal macroscopic cohesive behavior. J Mech Phys Solids 50:1727–1741
33. Oh DJ, Johnson RA (1992) Simple embedded atom method model for fcc and hcp metals. J Mater Res 3(3):471–478
34. Puska MJ, Nieminen RM, Manninen M (1981) Atoms embedded in an electron gas: immersion energies. Phys Rev B 24(6):3037–3047
35. Puska MJ, Nieminen RM (1983) Atoms embedded in an electron gas: phase shifts and cross sections. Phys Rev B 27(10):6121–6128
36. Qian J, Li S (2011) Application of multiscale cohesive zone model to simulate fracture in polycrystalline solids. ASME J Eng Mater Technol 133:011010
37. Schlick T (2002) Molecular modeling and simulation: an interdisciplinary guide. Springer-Verlag New York, Inc., Secaucus
38. Tadmor M, Ortiz EB, Phillips R (1996) Quasicontinuum analysis of defects in solids. Philos Mag A 73(6):1529–1563
39. van den Bosch MJ, Schreurs PJG, Geers MGD (2006) An improved description of the exponential Xu and Needleman cohesive zone law for mixed-mode decohesion. Eng Fract Mech 73(9):1220–1234
40. Xu XP, Needleman A (1994) Numerical simulations of fast crack-growth in brittle solids. J Mech Phys Solids 42(9):1397–1434
41. Yuan XJ, Chen NX, Shen J, Hu W (2010) Embedded-atom-method interatomic potentials from lattice inversion. J Phys: Condens Matter 22(37):375503
42. Yao H, Gao H (2007) Multi-scale cohesive laws in hierarchical materials. Int J Solids Struct 44(25–26):8177–8193
43. Zeng X, Li S (2010) A multiscale cohesive zone model and simulations of fractures. Comput Methods Appl Mech Eng 199(9–12):547–556